

# COMPUTATIONAL MODELING AND EXPERIMENTAL VALIDATION OF MICROSTRUCTURAL DEVELOPMENT IN SUPERALLOY CMSX-4 PROCESSED THROUGH SCANNING LASER EPITAXY

Ranadip Acharya, Rohan Bansal, Justin J. Gambone, Paul Cilino, and Suman Das

George W. Woodruff School of Mechanical Engineering, Georgia Institute of Technology,  
Atlanta, GA 30332

REVIEWED, Accepted August 22, 2012

## **Abstract**

This paper focuses on computational modeling of Scanning Laser Epitaxy (SLE), an additive manufacturing technology being developed at Georgia Tech for the creation of equiaxed, directionally-solidified or single-crystal structures in nickel-based superalloys. The thermal modeling of the system, carried out in a commercial CFD software package, simulates a heat source moving over a powder bed and dynamically adjusts the property values for consolidating CMSX-4 alloy powder. For any given position of the beam, the geometrical parameters of and the temperature gradient in the melt pool are used to estimate the resulting solidification microstructure. Detailed study of the flow field also revealed formation of rotational vortices in the melt pool. Microstructural predictions are shown to be in good agreement with experimental metallography. This work is sponsored by the Office of Naval Research through grant N00014-11-1-0670.

## **Introduction**

In order to improve the efficiency of gas turbine engines through higher operating temperatures, investment cast equiaxed turbine component parts are now often replaced by components that have either directionally solidified columnar or single crystal (SX) microstructural morphology. During the operation of these SX turbine blades, damage and wear at their leading tip occurs, limiting the lifetime of the SX components and necessitating the replacement of the numerous airfoils within the engines. Hence, it is of immense interest to develop a process which can restore the single crystal microstructure at the locations of damage and allow for the blades to be reused rather than be scrapped. The work presented here focuses on the development and modeling of a new process, Scanning Laser Epitaxy (SLE), by which high value SX components can be repaired. The SLE process is extensible to metal powder bed-based layer-by-layer additive manufacturing of superalloy components.

SLE is a laser-based additive manufacturing process for the creation of structures in equiaxed, directionally solidified and single-crystal nickel superalloys through the selective melting and re-solidification of superalloy powders. In SLE, a tightly focused laser beam is guided by a high-speed galvanometer scanners allowing for tight control of the amount of energy being applied to the top of the powder bed, as well as the speed at which the melt pool moves across the substrate. Under the proper operating conditions and with sufficient substrate meltback, the solidification microstructure follows the morphology of the underlying substrate, allowing for directional and even SX growth.

Several reports on the modeling aspects of laser cladding-based additive manufacturing approaches can be found in the literature. Approaches based on Finite Element Methods (FEM) and Finite Volume Methods (FVM) are employed for the thermal modeling of the system [1, 2]. Gaumann coupled the Columnar to Equiaxed Transition (CET) modeling with the Rosenthal solution in earlier work based on laser cladding [3]. Rappaz et. al. provided a detailed modeling of the microstructure/columnar orientation based on the solidification velocity and crystalline orientation [4]. This approach is based on the selection of the growth direction that closely follows the melt pool normal direction. Later on, substrate orientation is also taken into account [5, 6].

In the current work, the laser beam moving across the x and y-directions is modeled as a line source scanning in x-direction. The power profile in the y-direction is formulated from the transient averaged data for a single scan and fitted with a 10<sup>th</sup> degree polynomial. The complete scan pattern is formulated. The associated melting and re-solidification of CMSX-4 powder bed and substrate is formulated by the equilibrium phase change model. Heat transfer to the base plate is also modeled using the heat conduction equation. Analysis of the flow-field modeling reveals the formation of rotational vortices due to the moving heat source and Boussinesq convection. The final melt pool information is used to predict the Oriented to Misoriented Transition (OMT) and CET. The complete simulation along with post-processing to predict the microstructure is performed in the ANSYS CFX modeling environment, which allows the integration of the thermal modeling with microstructure prediction. Reasonable agreement between the simulation and the experimental results is achieved.

### **Experimental**

The nickel-based superalloy CMSX-4 was chosen as the material to be used in this study of the SLE process. The CMSX-4 powder (composition listed in Table 1), was produced by Praxair Surface Technologies using an atomization process and had a particle size ranging from 85-150µm. Initially, the process was tested on rectangular SX cast CMSX-4 coupons having dimensions of 35.56mm x 10.16mm x 2.54mm. Each substrate was placed into a 35.56mm x 10.16mm recess cut into an Inconel 625 base plate.

**Table I.** Chemical Compositions (wt%) of CMSX-4

Cr	Co	Mo	Re	W	Al	Ti	Ta	Hf	Ni
7.6	9.3	0.4	1.0	2.0	12.6	1.3	2.2	0.03	Bal

During preliminary testing the powder was deposited in various thicknesses, between 1 and 2mm, to find the ideal height of deposit. The powder was held in place above the substrate using wells cut into a ceramic foam. After the samples were prepared, they were placed into an atmospheric process chamber which was then purged with argon. A 1064nm 2kW Nd:YAG laser beam was used in conjunction with a Cambridge Technologies galvanometer scanner to focus the beam to 1.5mm diameter at the top of the substrate. A raster scan pattern across the width of the sample was used to propagate a linear melt pool across each substrate. Three variables were altered between each experimental run: laser power, scan speed, and the number of repeated

scans at the start of the raster pattern. Table II lists the operating ranges for each of the parameters.

**Table II.** Process parameter ranges found to produce well formed CMSX-4 deposits.

Process Parameter	Range
Powder Thickness	1 – 1.5 mm
Laser Power	400 – 600 W
Scan Speed	150 – 250 mm/sec
Initial Repeat Scans	50 – 150

The laser power and scan speed were both varied to control the energy being applied to the sample during the raster scan pattern. Sufficient preheat was required in order to form a proper fusion bond across the whole substrate. Without a high enough preheat the melt pool would not wet the surface of the underlying substrate and voids were formed along the interface.

### Microstructural Investigation

Each sample was sectioned along the length and width to visualize the microstructure in orthogonal directions. Using a Buehler automated saw, each sample was first cut lengthwise, and then sectioned by multiple widthwise cuts. Imaging was then completed using a Leica DM6000 optical microscope at 100x magnification.

As demonstrated by the sample in Figure 1, many sections showed a full metallographic bond along the entire length of the sample. The transition from the cast CMSX-4 substrate to the laser processed material is indicated by the sharp reduction in dendrite spacing.

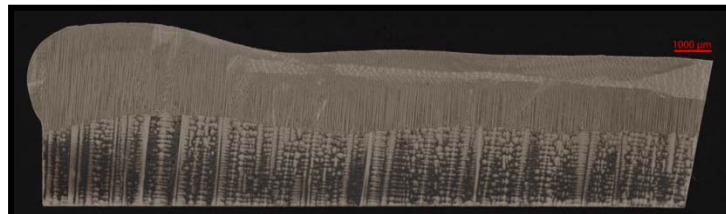


**Figure 1.** Representative lengthwise section of the first half of a CMSX-4 sample with the starting edge on the left side of the image

Figure 2(a) provides a detailed view of the transition from the columnar morphology to equiaxed/polycrystalline morphology, known as the columnar to equiaxed transition (CET). This columnar to equiaxed transition (CET) is due to the increase in isotherm velocity near the surface and a decrease in the temperature gradient which causes the formation of a constitutionally undercooled zone [3]. Figure 2(b) provides a detailed view of the transition from single crystal growth with [001] directionality to a shift in orientation. This change is known as oriented to misoriented transition (OMT) and is caused by a change in direction of the temperature gradient as the substrate becomes increasingly hot toward the end of the scan.



**Figure 2.** (a) Columnar to equiaxed transition and (b) Oriented to Misoriented transition

### Thermal Modeling

A transient, multi-domain model with temperature dependent property values is used to simulate the thermal aspect of the model and to predict the melt depth. Thermo-physical property data for liquid and solid CMSX-4 is accurately modeled using tabular data [7]. The multi-domain model consists of CMSX-4 domain (Consisting of the substrate as well as the powder deposit), the excess powder surrounding the melt pool, and the Inconel 625 base plate. The Inconel 625 property data is also modeled using tabular data [8]. Figure 3 shows the different domains involved. The mesh for the given problem is generated in ANSYS Mesher. The node count for the given case is around 250k with skewness not exceeding 0.5. The problem is solved in finite volume-based CFD solver ANSYS CFX.

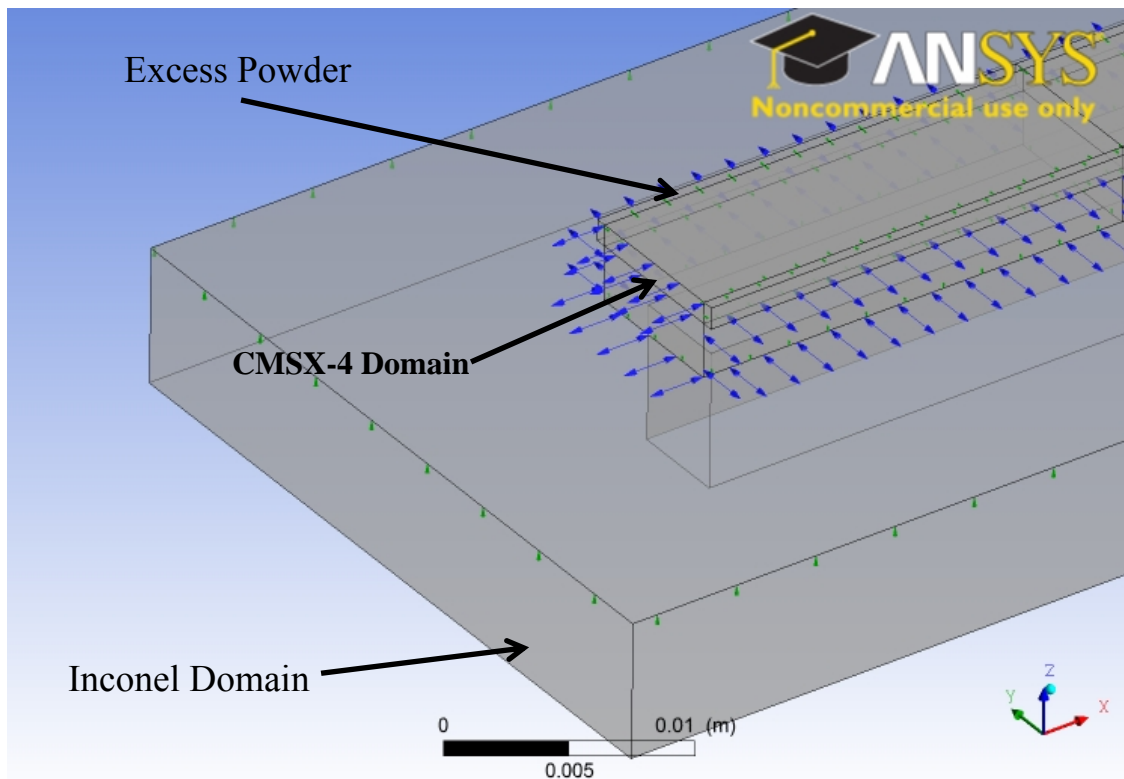


**Figure 3.** CFX multi-domain model showing different domains in CFD model

The solid and liquid component enthalpy equations, expressed in terms of volume fraction,  $r$ , are:

$$\frac{\partial(\rho_s r_s h_s)}{\partial t} + \nabla \cdot (\rho_s r_s \underline{U}_s h_s) = \nabla \cdot (r_s k_s \nabla T_s) + I \quad (1a)$$

$$\frac{\partial(\rho_L r_L h_L)}{\partial t} + \nabla \cdot (\rho_L r_L \underline{U}_L h_L) = \nabla \cdot (r_L k_L \nabla T_L) - I \quad (1b)$$

Here  $\rho$  is the density,  $h$  is the enthalpy (including the latent heat),  $T$  is temperature,  $\underline{U}$  is velocity and  $I$  is the interphase heat transfer. The subscripts  $S$  and  $L$  refer to the solid and liquid components respectively.

Equation (1a) and (1b) can also be expressed more compactly as:

$$\frac{\partial(\bar{\rho}h)}{\partial t} + \nabla \cdot (\bar{\rho}\underline{U}h) = \nabla \cdot (\bar{k}\nabla T) - \nabla \cdot (\bar{\rho}Y_s(\underline{U} - \underline{U}_s)(h_L - h_s)) + S \quad (2)$$

Where  $\bar{\rho}$  is mixture density,  $h$  is the mixture enthalpy,  $\bar{k}$  is mixture conductivity,  $Y_s$  is the mass fraction of solid [9].

The final term of Equation (2) represents an additional source due to the difference in velocity between the solid and liquid components. This term is finite only in the mushy region of the flow ( $0 < Y_s, Y_L < 1$ ). In regions of pure liquid or pure solid, the mixture enthalpy equation is identical to the appropriate component enthalpy equation. The volume fraction of liquid and solid component is incorporated using accurate tabular data representing solid fraction of CMSX-4 in the melting range. In order to consider the resistance to flow in the mushy region a Darcy like source term is incorporated. The permeability is modelled using Kozeny-Carman equation [10].

$$\underline{S}_M = \min\left(C, \frac{\mu_L (1 - r_L)^2}{K_0 r_L^3}\right)(\underline{U} - \underline{U}_s) \quad (3)$$

To prevent division by zero, the term is bounded by a user-specified maximum,  $C$ .

In the turbulence equations, sink terms similar to the Darcy terms in the momentum equation are applied to damp the turbulence in solid regions. For the  $k$ - $\epsilon$  model, these take the form [9]:

$$S_k = -\frac{\mu_L (1 - f_L)^2}{K_0 f_L^3} k \quad , \quad S_\epsilon = -\frac{\mu_L (1 - f_L)^2}{K_0 f_L^3} \epsilon \quad (4)$$

For the other two domains solid conduction equation is solved:

$$\rho \frac{\partial(\rho H)}{\partial t} = \nabla \cdot (K \nabla T) + S_0 \quad (5)$$

Where,  $\rho$  =Density,  $H$ =Enthalpy,  $K$ =Thermal conductivity,  $S_0$ =Source/sink.

Since there is no flow into or out of the domain, the chosen model prevents the use of an explicitly varying density for liquid CMSX-4. Therefore the volumetric changes are accounted for using the Boussinesq approximation to artificially include a buoyancy induced source term.

The actual laser heat source has a Gaussian beam radius of 0.75 mm. The spatial profile in the y-direction as the laser beam completes one scan is averaged over a single scan length over the sample width and fitted with a 10<sup>th</sup> degree polynomial. This particular profile is then used as a line source with Gaussian distribution applied in x-direction. This constitutes the term S in the equation (2). The conservation of H-energy is assured at all connecting interfaces. The convection heat loss is modeled using Newton's law of cooling as a surface sink term applied at all interfaces open to surroundings. Radiation loss is also modeled from open surfaces using sink term. The transient model is solved using a timestep value equal to 0.00215 s. The inclusion of convection, phase change model and Darcy sink term together necessitated the use of a lower timestep value in order to ensure the solver stability. The imbalance in the system is kept within 1% and the convergence ensures the RMS value of residual to below 1e-4.

Once solved, the result is post-processed in CFD-post to analyze the melt pool nature, the melt depth profile and the temperature distribution. The convection modeling allowed visualizing the velocity and vorticity field. For comparison purposes, pure conduction modes are also run with same set of parameters and the results are compared to distinguish the effect of convection on melt depth and microstructure.

### Results and Discussion

The melt depth profile is of particular importance for the present application and hence compared with the actual micrograph. Reasonable quantitative agreement is achieved in the simulated profile and observed data as shown in Figure 4(a) and Figure 4(b) for two different powder thickness and operating parameter sets.

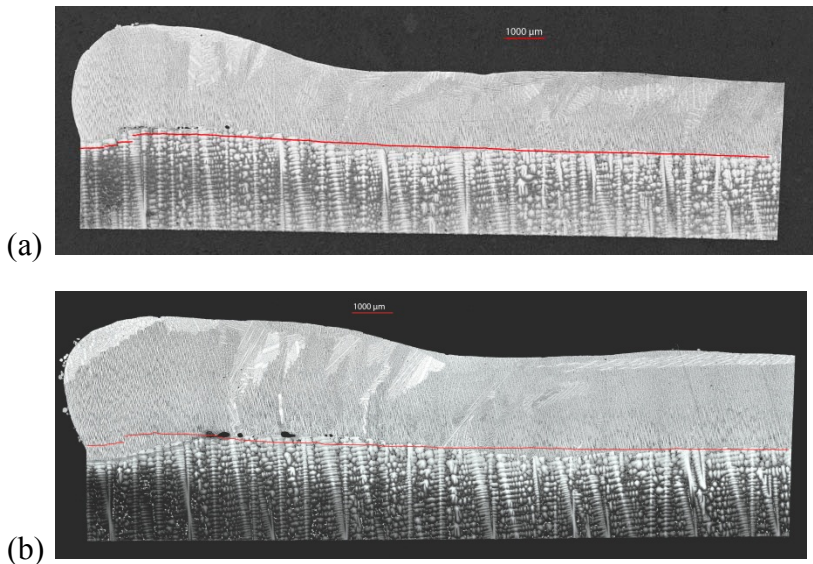


**Figure 4.** Comparison of the simulated meltdepth (Red line) with actual micrograph for (a) powder thickness = 1 mm and (b) powder thickness = 1.5 mm

In order to understand the effect of convection on the estimated melt depth, simulations without incorporating fluid convection are carried out and comparisons are drawn with actual melt depth

profile. As seen in Figure 5, the discrepancy is centered at the starting edge and begins to dissipate as the scan progresses. However, it is found that at any position of the heat source incorporation of convection results in a decrease of melt pool of area by around 10%.

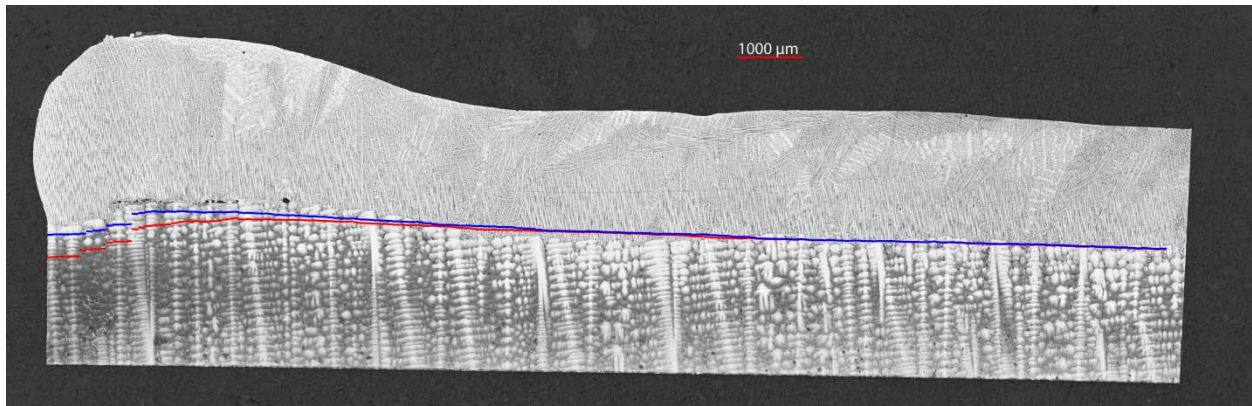


**Figure 5.** Comparison of the melt depth with actual micrograph for models without convection (red line) and with convection (blue line)

The effect of convection on the mushy zone is also studied and compared in Figure 6. As shown, the extent of the mushy zone decreases by around 30% due to the inclusion of convection.

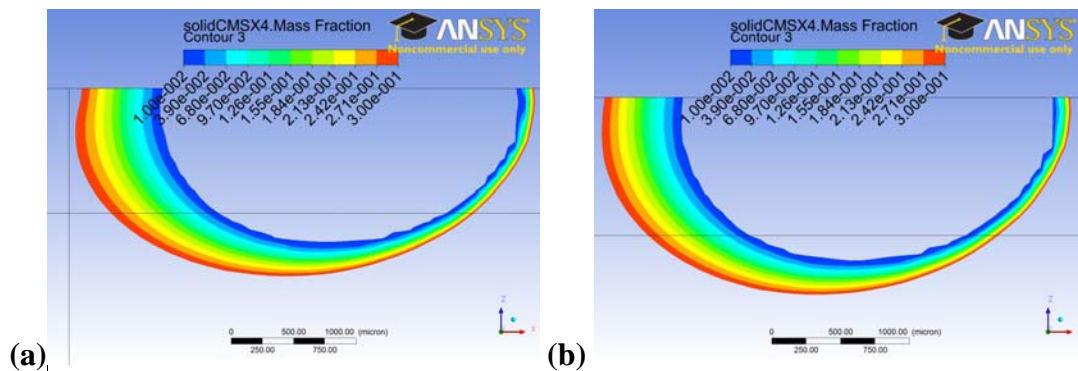


**Figure 6.** Extent of the mushy zone (a) without convection and (b) with convection

However, the most significant effect of convection is observed on the temperature gradient profile at the solid-liquid interface. As shown in Figures 6, the melt pool takes a convex hull shape in the raster scan scenario instead of an ellipsoidal profile, as has been observed by others in single bead scans of laser cladding. As seen from Figure 7, inclusion of convection results in a decrease in the range of temperature gradients over the melt pool. As a result, the maximum temperature gradient decreases and the minimum value observed increases. However, the maximum value is always observed ahead of the heat source, in a region which will undergo remelting as the scan progresses. The region that lies behind the heat source is of importance and this region experiences increased temperature gradient due to inclusion of convection.

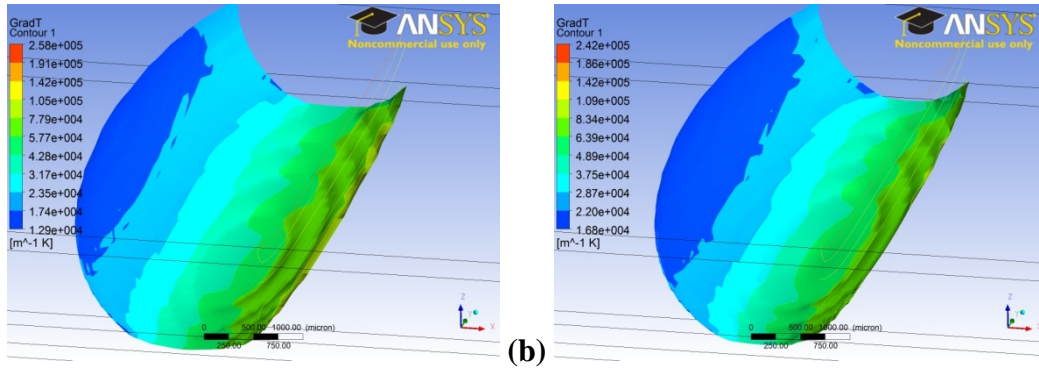


**Figure 7.** Temperature gradient at the solid liquid interface (a) without convection and (b) with convection

The velocity field generated due to the moving heat source is of importance to understand how loose powders are drawn into the melt pool. As shown in Figure 8 (a), the flow field generated consists of two vortices with the center of the vortex at lower velocity. The center is located at the middle of the melt pool and the flow field draws loose powder at the top while the melt pool expands at the bottom and sideways. The moving heat source also results in an outgoing high temperature current at lower velocity as shown in Figure 8 (b).

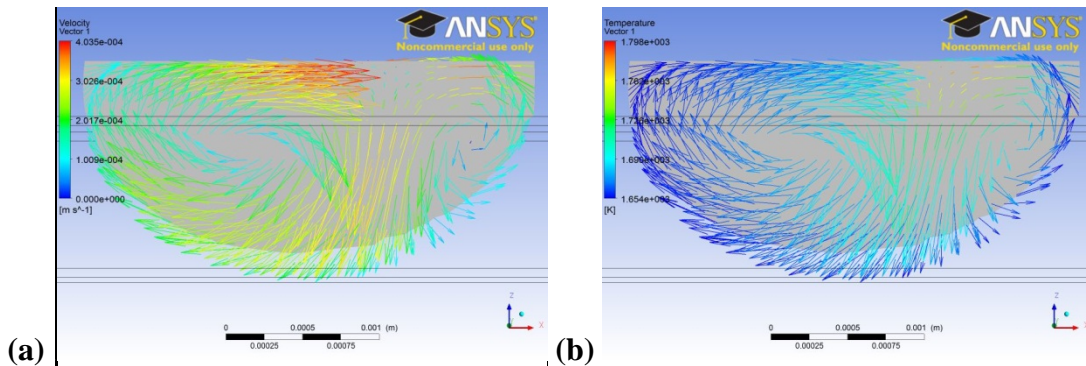


**Figure 8.** (a) Velocity vector observed in the liquid region and (b) Temperature map of the velocity vector in the melt pool.

The presence of the curl component of the velocity vector in Figure 9 indicates that the flow field comprises of rotational vortices in the given case.

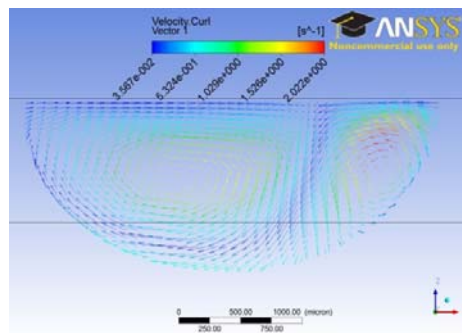


**Figure 9.** Vorticity vector in the melt pool

## Microstructure Modeling

Modeling of solidification microstructure is conducted particularly to understand the following two aspects of SX alloys – (a) OMT and (b) CET.

(a) OMT Modeling:

1. In order to resolve the columnar orientation it is necessary to take the normal component of the solid-liquid interface and then take the inner product of this normal component with the (100), (010) and (001) direction vectors.
2. The maximum value of the inner product provides the minimum of the cosine component of the inclination angle between the two directions.

Hence,

$$\cos \psi_k = \max(\hat{n} \cdot \hat{u}_k)$$

( $\hat{n}$  = normal vector to the solid liquid interface and  $\hat{u}_k$  = Direction vector)

3. The orientation vector for (001) is assigned a value of 1. The (001) and the (100) vector are assigned values of 10 and 100, respectively. A value of zero indicates the possibility of conflicting columnar orientations.

The plot of the orientation vector is shown in Figure 10 for two different operating parameter sets. Clearly, the flip in direction (from 001 to 100) is suggested in the plot as evidenced in the lengthwise section of the samples. However, Due to the approximation of power profile in the y-direction, the 010 orientation cannot be described.

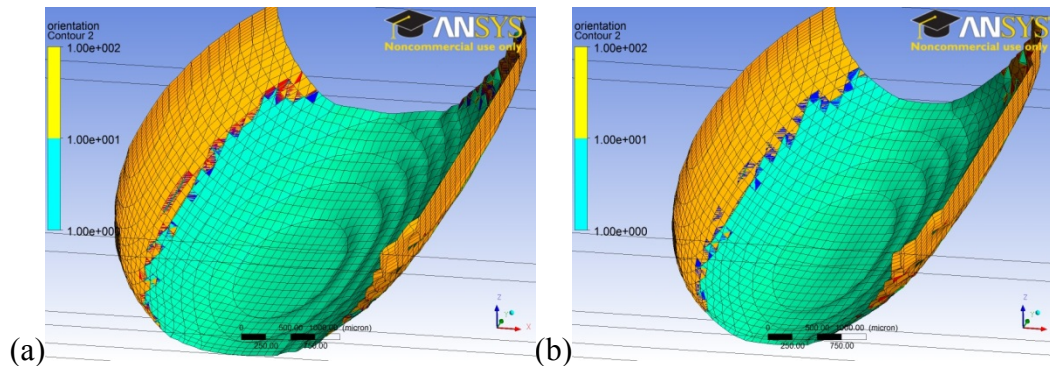


**Figure 10.** Orientation vector plot showing OMT for two different operating parameters.

(b) CET Modeling:

The CET modeling is done in the following steps:

1. The Temperature gradient at the solid-liquid interface ( $G$ ) is evaluated from CFD model.
2. The solid-liquid interface orientation ( $\theta_i$ ) is evaluated from  $\theta_i = \cos^{-1}(G_i/G)$  (for  $i=x, y, z$ )
3. The growth rate of the solid-liquid interface is given by  $V = S \cos \theta$  ( $S$ = scan speed/Line source speed)

4. the temperature gradient parallel to the dendrite growth direction,  $G_{hkl}$ , is calculated using the equation  $G_{hkl} = G/\cos \psi$ ;
5. The dendrite growth velocity,  $V_{hkl}$ , is calculated using the equation  $V_{hkl} = S\cos\theta/ \cos \psi_k$ .
6. The Rappaz modification [4] is applied to predict CET as follows:

$$G_{hkl}^n / V_{hkl} \geq \sqrt[3]{\frac{-4\pi}{3 \ln(1-\phi)}} \sqrt{\frac{N_0}{n+1}} \left(1 - \frac{\Delta T_n^{n+1}}{\Delta T_{tip}^{n+1}}\right) \Delta T_{tip}$$

Where,  $n$ =material constant ( $n=3.4$  for CMSX-4),  $\phi$ =equiaxed fraction (critical value = 0.066%),  $N_0$ = nucleation density,  $\Delta T_{tip}$ =tip undercooling,  $\Delta T_n$ = nucleation undercooling.

7. A lower value of the left hand side increases  $\phi$  for a given nucleation density. Hence, a lower value of this ratio indicates the likeliest location of columnar-to-equiaxed transition.

Figure 11 shows the plot of the  $G_{hkl}^n / V_{hkl}$  ratio for the same sample at two different positions of heat source. Here only the portion of the melt pool lying behind the heat source is compared. As seen, the value varies by five orders of magnitude with position. This explains the random nature of the stray grain formation for this sample as seen. The CET parameter is lower for the 2<sup>nd</sup> position and the experimental micrograph in Figure 12 also shows CET at lower height for position 2.

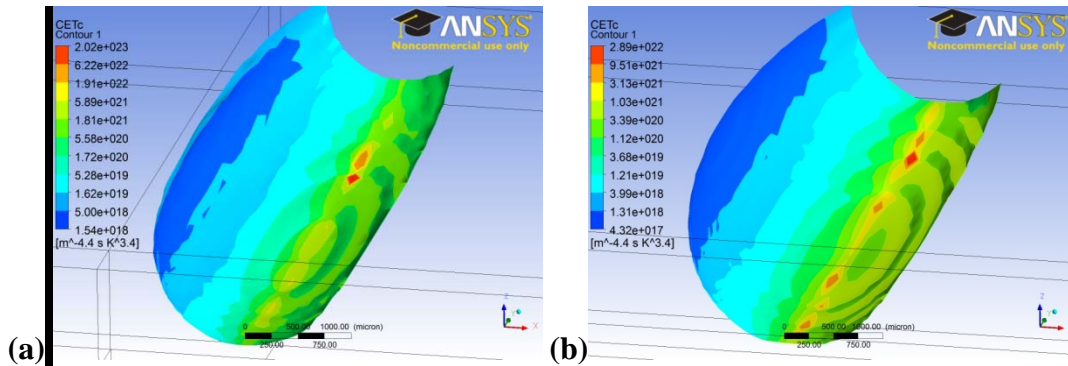


**Figure 11.** CET criterion plot for same sample at (a) heat source position 1=7.9 mm and (b) heat source position 2=10.1 mm

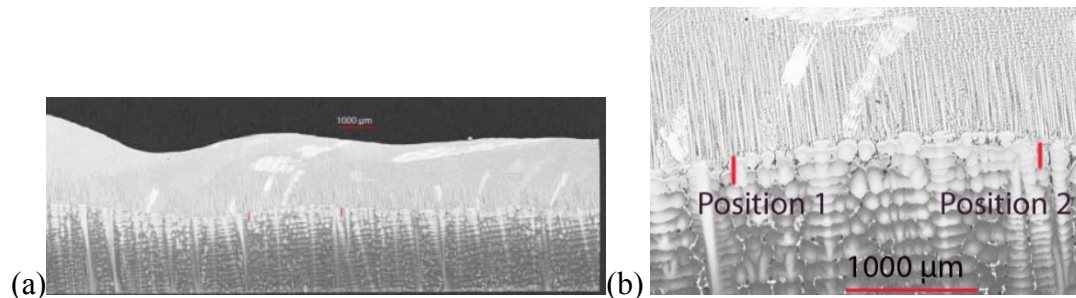


**Figure 12.** (a) Experimental micrograph for the given sample showing CET and (b) closer look at the CET for the given position showing larger columnar height for position 1.

## Conclusion

In the current work, a modeling scheme has been implemented to simulate the SLE process using a single platform. The model is able to predict the complete temperature distribution and melt pool behavior. Inclusion of convection modeling provides insights on the flow field established in the melt pool and how the loose powders are drawn inside melt pool. It is shown that the flow field comprises of two rotational vortices. The same platform also allows the modeling of solidification microstructure to predict the OMT and CET. The melt pool behavior for raster scanning situation is investigated. The final aim would be to develop a processing map based on the CET criteria that will allow us to predict the microstructure beforehand. However, the current simulation still allows us to find out the possibility of getting CET and OMT as well as the most likely locations of their occurrence. The simulation shows reasonable qualitative agreement with the experimental data in predicting the CET. However, the inclusion of Marangoni convection and the determination of CET criterion from experimental studies is necessary to obtain quantitative data for microstructural investigation e.g. columnar to equiaxed ratio.

## Acknowledgments

This work is sponsored by the Office of Naval Research through grant N00014-11-1-0670.

## References

- [1] T. D. Anderson, J. N. DuPont, and T. DebRoy, "Origin of stray grain formation in single-crystal superalloy weld pools from heat transfer and fluid flow modeling," *Acta Materialia*, vol. 58, pp. 1441-1454, 2010.
- [2] T. H. C. Childs, C. Hauser, and M. Badrossamay, "Mapping and Modelling Single Scan Track Formation in Direct Metal Selective Laser Melting," *CIRP Annals - Manufacturing Technology*, vol. 53, pp. 191-194, 2004.
- [3] M. Gaumann, "Epitaxial Laser Metal Forming of a Single Crystal Superalloy," PhD Thesis, EPFL Lausanne, 1999.
- [4] M. Rappaz and C. A. Gandin, "Probabilistic modelling of microstructure formation in solidification processes," *Acta Metallurgica et Materialia*, vol. 41, pp. 345-360, 1993.
- [5] S. Mokadem, C. Bezençon, A. Hauert, A. Jacot, and W. Kurz, "Laser Repair of Superalloy Single Crystals with Varying Substrate Orientations," *Metallurgical and Materials Transactions A*, vol. 38, pp. 1500-1510, 2007.
- [6] W. Liu and J. N. DuPont, "Effects of substrate crystallographic orientations on crystal growth and microstructure development in laser surface-melted superalloy single crystals. Mathematical modeling of single-crystal growth in a melt pool (Part II)," *Acta Materialia*, vol. 53, pp. 1545-1558, 2005.
- [7] T. Matsushita, H.-J. r. Fecht, R. K. Wunderlich, I. Egry, and S. Seetharaman, "Studies of the Thermophysical Properties of Commercial CMSX-4 Alloy†," *J. Chem. Eng. Data*, vol. 54, pp. 2584-2592, 2011.
- [8] S. J. D. Matthew J. Donachie, *Superalloys, A Technical Guide*: ASM International, 2003.
- [9] I. Hamill, "Implementation of a Solidification Model in CFX-5," CFX Ltd.2003.
- [10] W. L. S. McCabe, Julian C.; Harriot, Peter, *Unit Operations of Chemical Engineering*, 7 ed. New York: McGraw-Hill, (2005).